Supporting Information for

Flow of wormlike micellar solutions over concavities

Fabian Hillebrand*[a], Stylianos Varchanis[ab], Cameron C. Hopkins[a], Simon J. Haward[a], and Amy Q. Shen[a]

[a]Micro/Bio/Nanofluidics Unit, Okinawa Institute of Science and Technology Graduate University, Onna-son, Kunigami-gun, Okinawa, 904-0495, Japan.
[b]Center for Computational Biology, Flatiron Institute, Simons Foundation, New York, NY 10010, USA.

S1 Interface width

The experimental fluid and the Giesekus constitutive model used in this study appear to be shear-banding based on the flow curve in Fig. 2 (a). However, in both cases we expect an interface between any two shear bands and the question arises if this affects the flow. In particular, the interface will influence the flow if its width is sizable compared to the channel width W [1] and will in the extreme case completely eliminate any shear bands. Here we look at the width of this interface by considering the channel flow as shown in Fig. S1. This follows our typical situation where we have a low shear band next to a high shear localization, whether it is at the wall or next to another low shear band. We estimate this interface width by considering the extrema of the third-derivative of the velocity profile, following the work of Cheng *et al.* [2] in the context of a Taylor-Couette flow. We use fifth-order spline interpolation to evaluate the third-order derivative in both experiment and simulation. The estimated interface widths for $Wi \geq 5$ match up to an error likely due to the interpolation, as should be expected for a shear-banding fluid. However, we find that that these predicted interface widths are underestimating the apparent interface width. As such, we have increased the estimate for the simulation by a factor 4 and the experiment by a factor 2. We find that in simulation it accounts for around 4% of the channel width and around 7% in the experiments, though this is heavily affected by noise related to the μ-PIV setup. For the experimental data, we use the time-averaged μ-PIV data located upstream of the lip vortex at the re-entrant corner of the expansion phase. We typically observe two regions of low shear next to each other away from the wall, with one corresponding to the bulk flow and the other to a vortex. In this case, the shear localization between the two low shear regions is twice the estimate giving interface widths of around $0.08W$ and $0.14W$. These interface widths are large compared to some of the concavities considered and we expect to observe some influence from the interface in these cases.

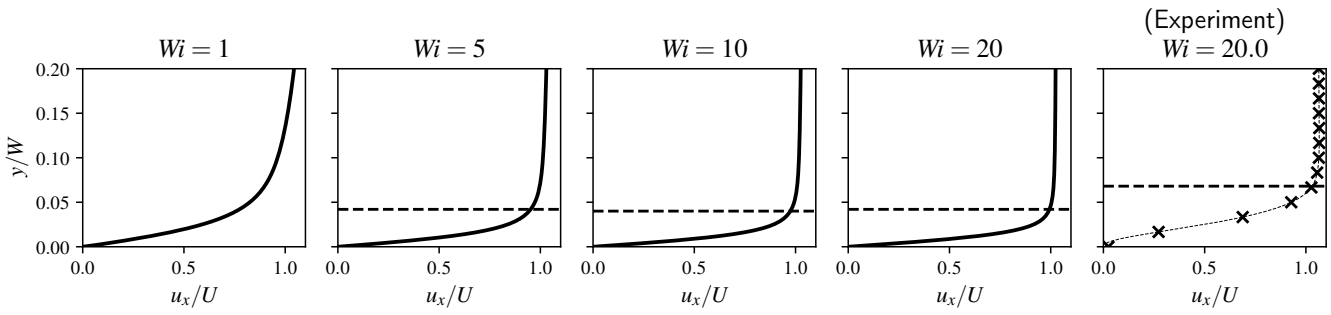

Figure S1 Flow profiles at various Wi values and indicated interface width at the wall for a channel flow with width W. The interface width, predicted to scale as the square root of the stress diffusion D_s, appears to be around $0.04W$ in the simulation and around $0.07W$ for the experiment. The simulations use a straight channel while the experimental data is taken upstream of the lip vortex located at the re-entrant corner of the expansion phase. Note that the experimental data is affected by noise related to the μ-PIV setup, particularly in close proximity to the wall.

S2 Simulation convergence

We show the mesh convergence for a square cavity ($L = W$, $D = W$) in table S1 for the mean squared velocity $\langle u^2 \rangle$ and elastic potential energy E_{el} as we increase the number of elements. We use the mesh with 393 216 elements (marked by '$*$') for the results of our study. Table S1 further shows a single consistent refinement of this mesh (marked by '$**$'), obtained by splitting every triangle into four triangles using the midpoints of the sides. We emphasize that while this is possible for this cavity, for larger cavities or expansion-contractions this poses a computational limitation on our simulations. For consistency between the different geometries, we use the same grading throughout our study as is presented here for the square cavity. The coarser meshes listed in table S1 use the same grading scheme as the mesh used to acquire the simulation data. Note that due to our grading scheme, see Fig. 3, the resulting finite element spaces are not nested. Overall, we observe that the error increases for larger Weissenberg numbers.

Table S1 Convergence in the mean squared velocity and elastic potential energy at different Weissenberg numbers for a square cavity ($L = W$, $D = W$) with respect to the number of elements and the degrees of freedom. The mesh resolution used for the simulations is marked by '$*$', with a consistent regular refinement marked by '$**$'

$\langle u^2 \rangle / U^2$	#Element	#DOF	$Wi = 0.1$	$Wi = 1$	$Wi = 10$
	6144	19 494	1.13067	0.99992	n/a
	24 576	75 846	1.13158	0.99971	0.98171
	98 304	299 142	1.13156	1.00029	0.98146
$*$	393 216	1 188 102	1.13149	1.00056	0.98163
$**$	1 572 864	4 735 494	1.13146	1.00063	0.98176
E_{el}					
	6144	19 494	5.06393	7.14035	n/a
	24 576	75 846	5.13005	7.27127	2.46290
	98 304	299 142	5.17192	7.40904	2.47626
$*$	393 216	1 188 102	5.19198	7.46662	2.49096
$**$	1 572 864	4 735 494	5.19873	7.48403	2.49880

S3 Comparison with rounded corner

In this section, we briefly compare the sharp corner we use in our study to a rounded corner with a radius $2 \times 10^{-2} W$, i.e., a curvature of $50 W^{-1}$. Generally, smoothing the corner influences the exact position of the shear localization and correspondingly the sizes of the flow structures. However, the biggest effect is on the lip vortex upstream of the expansion phase, which is further discussed in section S4. The overall flow structures inside the concavities are not significantly affected as is shown in Fig. S2 (a) & (c) for a square cavity and (b) & (c) for an expansion-contraction flow.

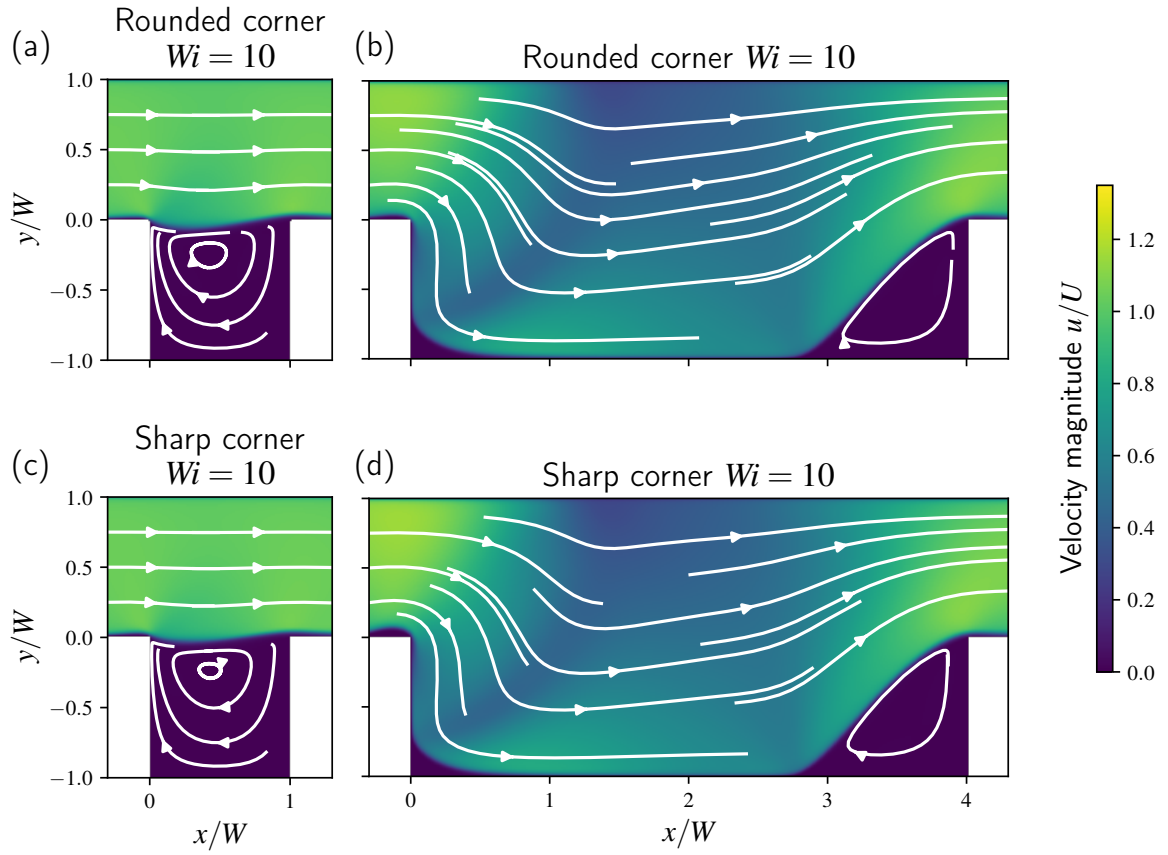

Figure S2 Velocity magnitude u and streamlines for (a) & (b) a rounded corner with a curvature of $50 W^{-1}$, and (c) & (d) a sharp corner used in the rest of our study. We compare (a) & (c) a square cavity as well as (b) & (d) an expansion-contraction at $Wi = 10$.

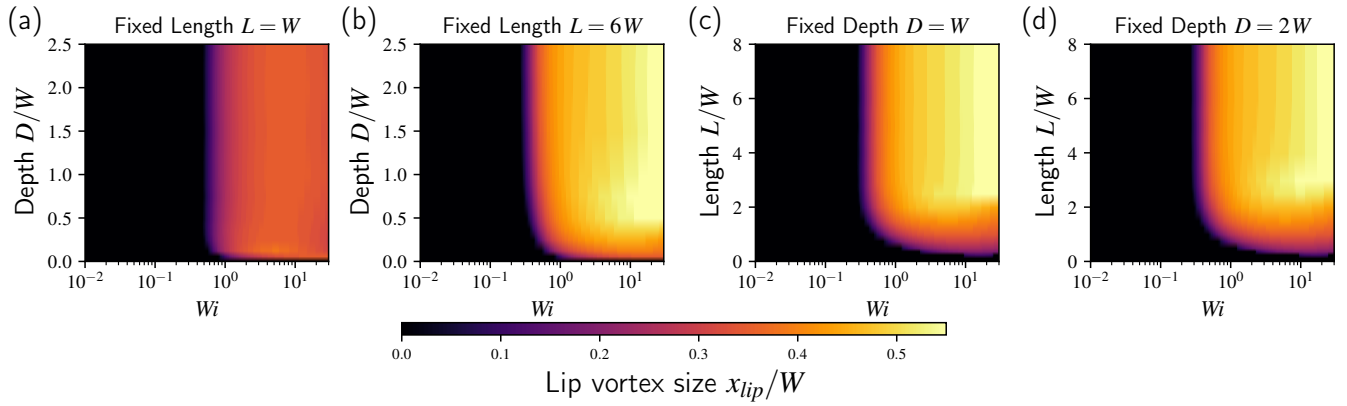

Figure S3 Lip vortex size x_{lip} over a range of Weissenberg numbers Wi for a fixed length (a) $L = W$ and (b) $L = 6W$ with varying depths, and for a fixed depth (c) $D = W$ and (d) $D = 2W$ with varying lengths. The data shown is based on the steady-state simulations and x_{lip} takes discrete values due to the applied extrapolation.

S4 Lip vortex sizes

Here we take a deeper look at the characteristics of the lip vortex that develops at the re-entrant corner upstream of the expansion plane as the Weissenberg number is increased. We focus on the steady-state simulations only since the lip vortex in the time-dependent simulation does not significantly differ on average from the steady-state value. Furthermore, even in the presence of multi-valued solutions at fixed Wi values from the pseudo-arclength continuation, the lip vortex retains its size and thus this does not pose an issue. Therefore, we show here the full data collected based on the pseudo-arclength continuation.

In Fig. S3 we present an overview of the lip vortex size x_{lip} as a function of Weissenberg number Wi. Fig. S3 (a) and (b) show x_{lip} as a function of cavity depth D at fixed values of cavity length $L = W$ and $L = 6W$, respectively. Fig. S3 (c) and (d) show x_{lip} as a function of L at fixed values of cavity depth $D = W$ and $D = 2W$, respectively. For any single sub-figure, we note that as the depth or length is increased, the lip vortex size x_{lip} starts to display a similarity solution, becoming independent of that parameter. Upon decreasing either parameter, the lip vortex disappears altogether as the straight channel is recovered. Additionally, we observe a general trend towards similar behaviors as either the fixed length or fixed depth is increased, which is illustrated by comparing Fig. S3 (b) and (d). Ignoring the onset for now, the lip vortex size x_{lip} eventually decreases with increasing Weissenberg number Wi for cavity flows, specifically for square or deep cavities, as is best illustrated by Fig. S3 (a). We attribute this decrease to the approximation to a lid-driven cavity and the associated shear localization. In particular, the curvature of the streamlines forming the lip vortex is decreased as the shear localization starts to cover the cavity, where the flow no longer infiltrates the cavity itself, leading to a decrease in the lip vortex size x_{lip}. This is in contrast to the expansion-contraction flows where x_{lip} continues to increase, albeit at a slower rate than at the onset, shown primarily in Fig. S3 (c) and (d).

The onset of the lip vortex follows a critical power-law of the typical form: $x_{lip} \sim (Wi - Wi_{crit})^{\alpha_{crit}}$, with critical Weissenberg number Wi_{crit} and critical exponent α_{crit}, before quickly deviating from this at larger Wi. The values of the critical parameters depend on the exact depth and length of the cavity, but we are still able to group them for cavity and expansion-contraction flows separately, as is shown in Fig. S4 (a) and (b), respectively. By extrapolating the limit for large lengths L for cavities or large depths D for expansion-contractions, we find a universal critical Weissenberg number $Wi^{\infty}_{crit} \approx 0.26$ and exponent $\alpha^{\infty}_{crit} = 0.70 \sim 0.75$ for both cases. This is consistent with the assumption that the limits $L \to \infty$ and $D \to \infty$ are uniform for the onset of the lip vortex, and hence commute. We emphasize that our results do not suggest that this applies to the overall flow structures. Instead, for example, we expect that applying the limit in length L followed by the depth D to result formally in an expansion and a contraction flow, whereas any other flow structure can be reached by fixing the aspect ratio D/L while taking the limits $L \to \infty$ and $D \to \infty$. However,

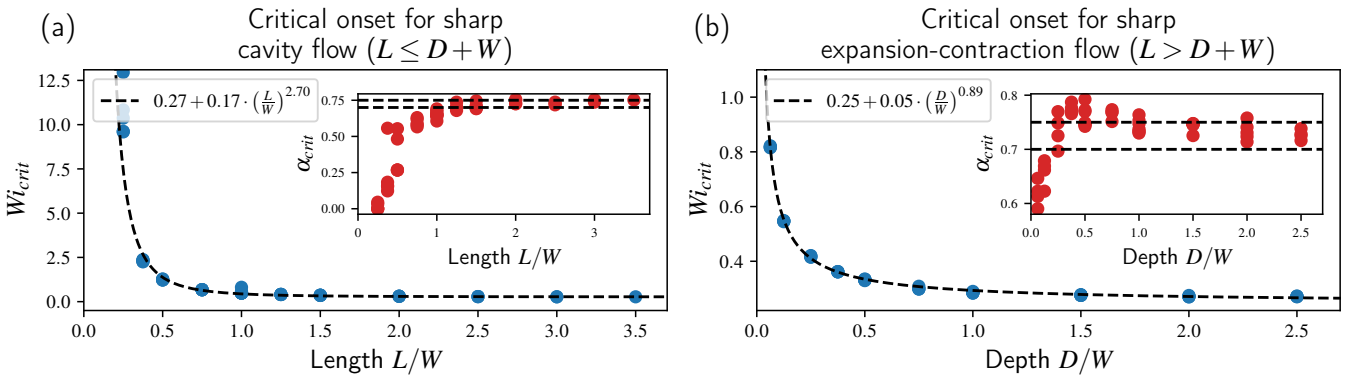

Figure S4 Estimated critical Weissenberg number Wi_{crit} and exponent α_{crit} for the onset of lip vortices using the simulations for (a) cavity flows ($L \leq D+W$) and (b) expansion-contraction flows ($L > D+W$). The critical behavior is given by $(Wi - Wi_{crit})^{\alpha_{crit}}$ and assumed to hold up to $Wi_{crit}+0.2$. The limit for Wi^{∞}_{crit} is extrapolated, while accounting for the spread in the data, using the model $Wi^{\infty}_{crit}+\gamma_b X^{\gamma_e}$, $X \in \{L/W, D/W, \}$, shown by the dashed line. For α^{∞}_{crit} we indicate the anticipated spread with dashed lines.

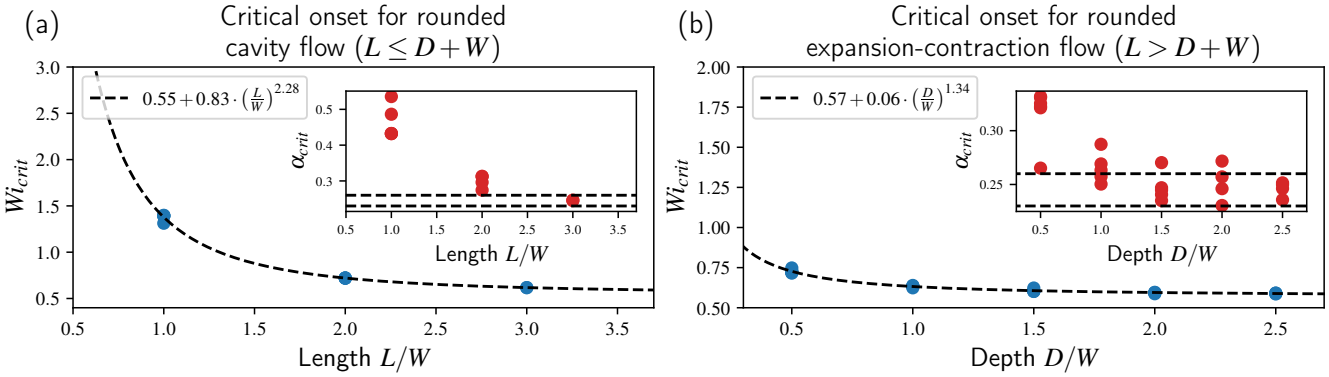

Figure S5 Estimated critical Weissenberg number Wi_{crit} and exponent α_{crit} for the onset of lip vortices using the simulations with rounded corners for (a) cavity flows ($L \leq D+W$) and (b) expansion-contraction flows ($L > D+W$) using rounded corners. We estimate a critical Weissenberg number $Wi^{\infty}_{crit} \approx 0.56$ with critical exponent $\alpha^{\infty}_{crit} \approx 0.25$. See also Fig. S4.

our results do imply an independence between the lip vortex and the flow structures inside the cavity or expansion-contraction in the limits.

In the limit of straight channels, the critical Weissenberg number Wi_{crit} diverges, which is expected as the straight channel does not exhibit a lip vortex, while the critical exponent α_{crit} appears to decay to zero. However, this last observation is not found for the smoothed corner, see Fig. S5, where we have run fewer simulations. Therefore, it is not entirely clear if such a trend is real or an artifact of fitting the critical exponent, which is sensitive to noise and the fitted Wi_{crit}. We note that the smoothed corner leads in general to a larger $Wi^{\infty}_{s;crit} \approx 0.56$ and a smaller $\alpha^{\infty}_{s;crit} \approx 0.25$. Thus, a smoothed corner reduces the lip vortex size, which agrees with the Pakdel-McKinley criterion,[3,4] as was previously proposed by Poole *et al.*[5] Moreover, we stress that the formation of a lip vortex is not due to shear localization and has also been predicted using models with neither shear-banding nor shear-thinning.[5,6]

S4.1 Comparison to experiment

For the lip vortex size x_{lip} we observe three regimes in the experiments, see Fig. S6, which is similar to the result by Hwang and collaborators[7,8] for the flow of a WLM solution in a sharp bend. At Weissenberg numbers less than 1.6, no lip vortex is observed in any of the three microchannels studied. The lip vortex then grows above the critical value $Wi_{crit} \approx 1.6$ with a time onset for the flow around $Wi \approx 11$. The time

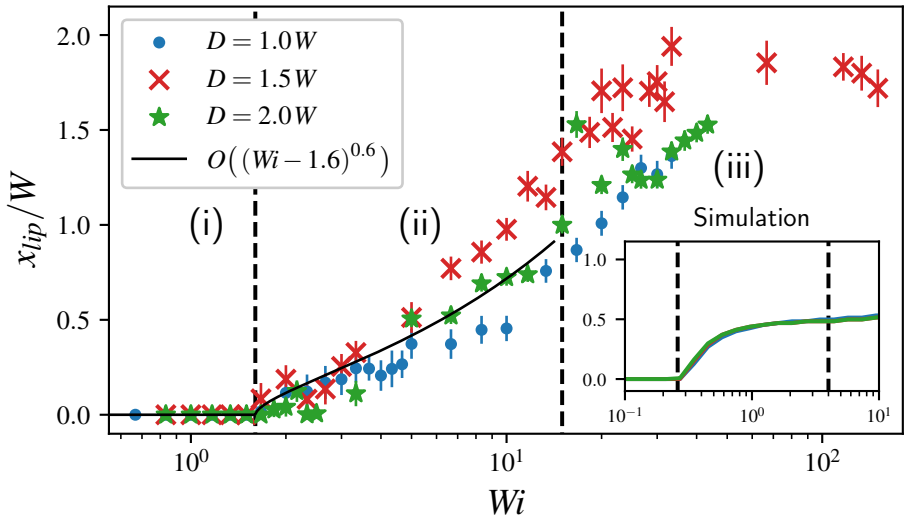

Figure S6 Experimental lip vortex size x_{lip} against Weissenberg number Wi for the different microfluidic devices. The vertical lines show the standard deviation in x_{lip} measurements obtained across velocity thresholds ranging from $0.1U$ to $0.4U$, with the symbol denoting the mean. Indicated are the three regimes: (i) no lip vortex, (ii) steady flow lip vortex, and (iii) unsteady flow lip vortex. The inset shows the steady-state simulated lip vortex sizes for comparable channel dimensions. We stress the different x- and y-axes between experiment and simulation.

dependence primarily appears in the bulk flow, while the lip vortex size x_{lip} measured at the wall does not necessarily change significantly. Overall, we observe that x_{lip} grows with increasing Wi and that it does not depend on cavity depth in the range $W \leq D \leq 2W$, which is in agreement with our simulations. Similar to the simulations, we also note a power-law increase for the lip vortex beyond its onset. This critical region is larger than it is for simulations with an estimated critical exponent $\alpha_{crit} \approx 0.6$, indicated as a solid black line in Fig. S6. We remark that the value of the lip vortex size x_{lip}, and thus also the critical exponent α_{crit}, depends heavily on the velocity threshold used to measure x_{lip}. Unlike in the simulations, the velocity cannot be extrapolated to the wall due to a lack of resolution. Instead, we consider the velocity magnitude compared to a threshold ranging from $0.1U$ to $0.4U$ at a distance of 2-3 pixels from the estimated wall, with the spread shown in Fig. S6.

S5 Pseudo-arclength continuation in short expansion-contractions

We have mentioned in the main text that there are some questions about the validity of the numerical solution given by the pseudo-arclength continuation. Here we take a second look at this focusing on the transitional regime, specifically short expansion-contractions, that caused the most numerical difficulties. We start by noting that the subcritical behavior observed in Fig. 5 (c) implies multiple steady-state solutions at some fixed Wi values. We have plotted these in Fig. S7 and the solution shown in (a) appears to be the most physically stable solution, given that it has the lowest elastic Helmholtz free energy. This is also the solution found by the first order continuation in this case but this solution does not always have the lowest elastic Helmholtz free energy. Furthermore, as we increase the Wi value the pseudo-arclength continuation can predict flow structures that appear to be nonphysical, see Fig. S8 (a). We are not entirely sure what causes this, but it may relate to the mesh resolution that becomes inadequate for large Wi or a potential failure of the solution method. Indeed, for the geometries with $D = 2W$ and $L = 3.5W$ as well as $D = 2.5W$ and $L = 4W$, both of which fall into short expansion-contractions, the mesh does not appear to be resolved fully for high Wi. In such cases, the pseudo-arclength continuation predicts several subcritical phenomena that in smaller geometries arise from too coarse meshes. We believe that this is the likely case also for $D = 1.5W$ and $L = 3W$ shown in Fig. S8 (a), while for $D = W$ and $L = 2.5W$ the flow is closer to S7 (c) even at higher Wi values, see Fig. S8 (b). On the other hand, it may also simply be a limitation of the Giesekus model and in a real system we would expect to observe time-dependence, similar to what is seen for the expansion-contraction flows. To fully answer the question on the validity at higher Wi, more sophisticated numerical methods are required to handle the computational cost, specifically memory requirement for large meshes, efficiently.

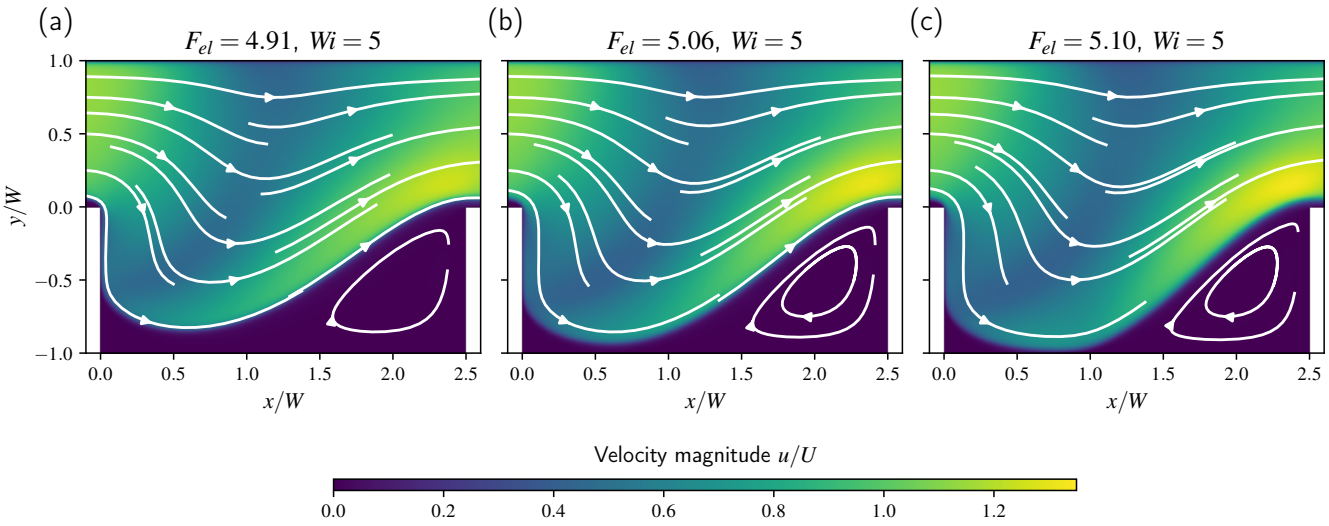

Figure S7 Velocity magnitude u and streamlines for the short expansion-contraction ($D = W$, $L = 2.5W$) at $Wi = 5$ using the pseudo-arclength continuation. We find three different solution with different elastic Helmholtz free energies: (a) $F_{el} = 4.91$, (b) $F_{el} = 5.06$, and (a) $F_{el} = 5.10$. These mainly differ in the position of the shear localization.

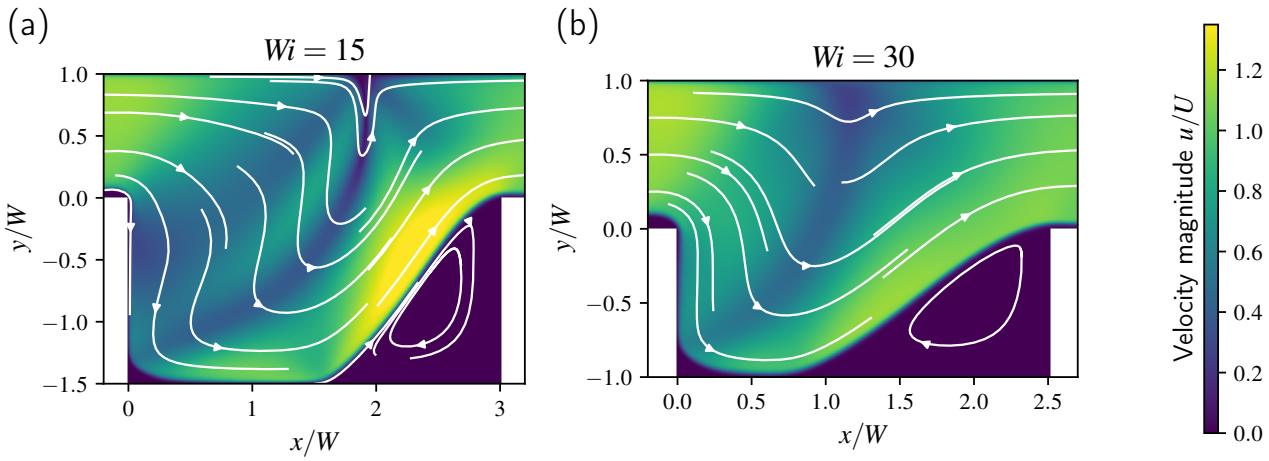

Figure S8 Velocity magnitude u and streamlines for the short expansion-contractions with (a) $D = 1.5W$ and $L = 3W$ at $Wi = 15$ and (b) $D = W$ and $L = 2.5W$ at $Wi = 30$ using the pseudo-arclength continuation long after the first order continuation fails. The predicted flow structures in (a) appear nonphysical, hinting at most likely issues with the mesh resolution at large Wi.

S6 Flow categories

In the main text we have shown several phase diagrams in Fig. 13 at fixed Wi values in terms of D and L. In Fig. S9 we show the complete data collected. Several additional flow structures are identified, such as the expansion-contraction flows with vertical lip vortices. Most data displayed uses the steady-state simulation with first order continuation. In cases where these failed to converge, we use the steady-state pseudo-arclength continuation instead. Note that there are some concerns about the validity of these, see section S5. The time-dependence is determined with separate unsteady simulations using a zero state (zero velocity, zero pressure, zero elastic stresses) as initialization. The flow rate is then gradually increased until reaching the desired value. The unsteady simulations are then run until a steady-state is reached or a periodic behavior became apparent.

References

1 C. Masselon, A. Colin and P. D. Olmsted, *Phys. Rev. E*, 2010, **81**, 021502.

2 P. Cheng, M. C. Burroughs, L. Gary Leal and M. E. Helgeson, *Rheologica Acta*, 2017, **56**, 1007–1032.

3 P. Pakdel and G. H. McKinley, *Phys. Rev. Lett.*, 1996, **77**, 2459–2462.

4 G. H. McKinley, P. Pakdel and A. Öztekin, *Journal of Non-Newtonian Fluid Mechanics*, 1996, **67**, 19–47.

5 R. J. Poole, F. T. Pinho, M. A. Alves and P. J. Oliveira, *Journal of Non-Newtonian Fluid Mechanics*, 2009, **163**, 35–44.

6 R. J. Poole, M. A. Alves, P. J. Oliveira and F. T. Pinho, *Journal of Non-Newtonian Fluid Mechanics*, 2007, **146**, 79–91.

7 M. Y. Hwang, H. Mohammadigoushki and S. J. Muller, *Phys. Rev. Fluids*, 2017, **2**, 043303.

8 Y. Zhang, H. Mohammadigoushki, M. Y. Hwang and S. J. Muller, *Phys. Rev. Fluids*, 2018, **3**, 093301.

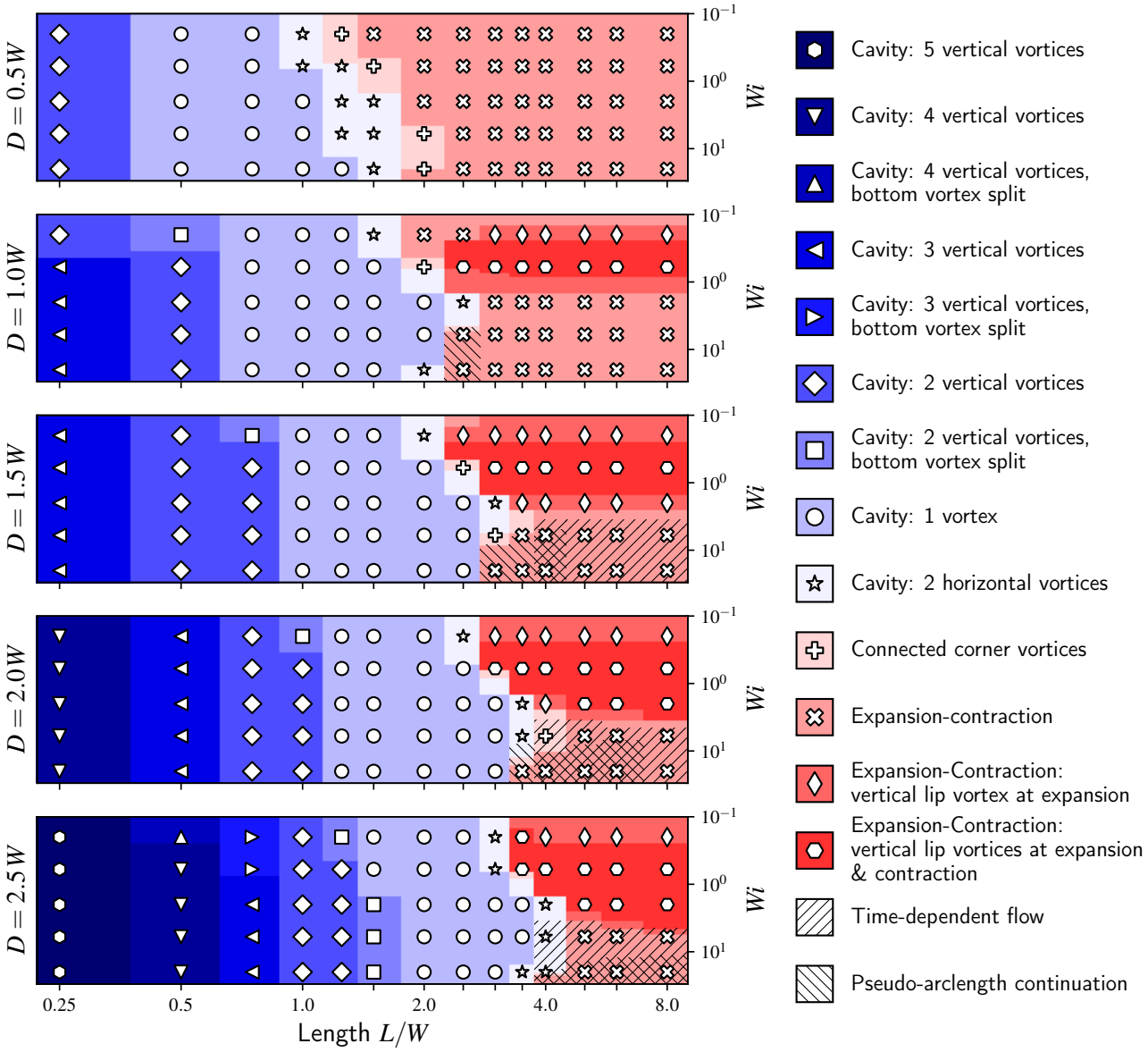

Figure S9 Phase diagrams in length L and Weissenberg number Wi for different fixed depths D based on the comprehensive numerical simulations (steady-state with first order continuation supplemented with the pseudo-arclength continuation where necessary and separate unsteady simulations at fixed Wi starting from zero). Time-dependent flow regimes are marked using an overlay with diagonals at a 45° angle. We further mark Wi values that require the pseudo-arclength continuation using an overlay with diagonals at a 135° angle. We differentiate thirteen different flows: five stacked vortices (⬢), four stacked vortices (▼) with bottom vortex split into two (▲), three stacked vortices (◀) with bottom vortex split into two (▶), two stacked vortices (◆) with bottom vortex split into two (■), a single vortex (●), two horizontal vortices (★), connected corner vortices (✚), and separated corner vortices (✖) with a vertical lip vortex at the expansion plane(⧫) or vertical lip vortices at both the expansion and contraction planes (⬣).